

Thermal transport characteristics of impinging ferrofluid droplets in the presence of a magnetic field

Ram Krishna Shah*

Mechanical Cluster, School of Advanced Engineering, UPES Dehradun, India - 248007

Abstract

Droplet interactions with solid surfaces are fundamental to natural phenomena and hold significant commercial relevance across diverse applications. While the impingement dynamics of conventional aqueous droplets on solid substrates are well-characterized, the behavior of non-aqueous droplets, particularly those influenced by external force fields like electric or magnetic fields, remains a less explored domain. This study addresses this gap by investigating the impact of a magnetic field on the impingement dynamics of ferrofluid droplets on a heated solid surface. Ferrofluids are unique colloidal suspensions of magnetic nanoparticles within a non-magnetic carrier fluid, enabling external manipulation of their dynamic properties through magnetic forces. The application of a magnetic field introduces an attractive force within the ferrofluid, fundamentally altering the droplet's spreading behavior and, consequently, its transport characteristics upon impact. Our findings reveal a substantial increase in both the maximum spreading diameter and the contact time between the droplet and the substrate, directly leading to enhanced thermal transport efficiency. Furthermore, the magnetic force effectively suppresses droplet bounce-off from hydrophobic surfaces. These critical parameters can be precisely controlled by adjusting the strength of the induced magnetic force. Such interactions can be used in the design of thermal switches and thermal management systems. The multi-physics interactions of magnetic fields, fluid flow, interface tracking, and heat transfer within the multiphase system are computationally modelled to examine the effect of Weber number and contact angle on maximum spreading and associated heat transfer characteristics.

Keywords: Ferrofluid, Magnetic field, Droplet impingement dynamics, Maximum spreading, Thermal transport

1. Introduction

Understanding droplet impingement on solid surfaces is essential across diverse fields, from spray cooling and coating processes to agriculture and disease transmission. Recent technological advancements, particularly in electronics miniaturization and heterogeneous integration, have driven the need for efficient thermal management due to increased heat flux generation. Spray cooling, utilizing the impact of numerous droplets, offers a promising solution^{1,2}. Optimizing this technique requires a fundamental understanding of individual droplet interactions with heated substrates, encompassing spreading, receding, rebound, and associated heat transfer mechanisms.^{3,4} These interactions are significantly influenced by droplet size, velocity, impact angle, and surface properties. Consequently, extensive research has focused on elucidating the impingement dynamics of aqueous droplets, leading to substantial advancements in our comprehension of these phenomena^{5,6}

While extensive research has explored the impact behavior of conventional aqueous droplets, the dynamics of droplets with unique properties, such as ferrofluids or ionic fluids, remain largely unexplored. Ferrofluids, colloidal suspensions of magnetic nanoparticles in a carrier liquid, offer intriguing possibilities for manipulating droplet behaviour through external magnetic fields, leading to their applications in microfluidics^{7,8}, heat transfer enhancement⁹⁻¹³, droplet manipulation platforms^{14,15}, and 3D printing¹⁶. Some of these applications necessitate a fundamental understanding of ferrofluid droplet interactions with substrates of varying wettability under magnetic influence. Consequently, recent investigations have begun to explore ferrofluid droplet impingement in magnetic fields. For instance, Ahmed et al.^{17,18} experimentally studied the effect of magnetic field strength (produced by permanent magnets of finite size) on the maximum spreading diameter, proposing semi-empirical correlations to predict such behaviour. They observed that the maximum spreading diameter could be tuned by varying the applied magnetic field strength without altering the Weber number, while the time to reach maximum spreading remained constant. Similarly, Zhou and Jing¹⁹ conducted experimental research on the impact dynamics of ferrofluid droplets under a vertical magnetic field. They reported a minimal effect of the magnetic field (non-uniform field created by an electromagnet) on the spreading diameter and oscillations. Hasan and Wang²⁰ studied the effect of vertically oriented uniform magnetic fields on the spreading dynamics of ferrofluid droplets on hydrophilic surfaces. They observed a decrease in maximum spreading diameter and an increase in droplet height with an increase in the intensity of the applied field strength. Li et al.²¹ proposed a theoretical model to predict the maximum spreading diameter for a wide range

of magnetic fields and Weber numbers and validated it against their experimental observations. They observed a decrease in the maximum spreading diameter till a critical Weber number and no effect thereafter, in the presence of a magnetic field. Huang et al. ²² developed a similar approach to predict the maximum spreading diameter and validated their model against their numerical results. Benter et al. ²³ conducted an experimental investigation to examine the effect of a magnetic field on impingement dynamics and the associated heat transfer characteristics of ferrofluid droplets. They observed significant enhancement (up to 2.5 times) in the heat transfer rate, especially for hydrophobic surfaces in the presence of the magnetic field.

It is evident from the literature review that a more comprehensive understanding is required regarding the influence of magnetic fields, especially for the non-uniform fields produced by realistic finite-size magnetic sources, on the maximum spreading of droplets across both hydrophobic and hydrophilic surfaces. Moreover, the crucial aspect of associated heat transfer has been addressed in only a single recent experimental study, highlighting a significant gap. Numerical modelling of these coupled phenomena promises valuable insights for numerous applications. To address this, the subsequent paragraphs present an in-depth literature review of the Phase-field (PF) methodology, the chosen approach for modelling contact line dynamics and fluid-fluid interface evolution in this work.

The Phase-field method is a diffuse interface (DI) method based on the free energy of the physical systems. It is a mathematical technique used to define and capture the dynamic evolution of the interfaces between multiple phases of the physical systems. PF methods were originally developed to capture phase transition phenomena, such as nucleation, evaporation, and solidification. More recently, PF methods have been used in diverse fields of applications such as phase transformation, solidification dynamics, fracture mechanics, multiphase flow, etc., for capturing the dynamic evolution of the interfaces and topological changes in multiphase systems ^{24,25}. In the context of binary fluid systems, PF methods represent a more physical approach to capturing the dynamics of the interfaces between the two fluids than other popular models, such as Volume of Fluid and Level Set methods, because of their free energy approach. The wetting and no-slip boundary conditions for moving contact line (MCL) problems can be easily implemented in PF modelling, unlike in Volume of Fluid and Level Set methods, where a workaround is required to avoid stress singularities at contact line motion ²⁵. Jacqmin first implemented the Cahn-Hilliard Phase-field (CH PF) model for the modelling of two-phase flows and moving contact line (MCL) problems ^{26,27}. He showed that such a model

can be successfully implemented in modelling interfacial flows. He also reported that the PF model's mobility parameter (γ) is a material-dependent property, and too large or too small a mobility would produce unrealistic results. A scaling relation for the mobility with the capillary width or interfacial thickness (ε) as $\gamma \sim \varepsilon^2$ was reported in his work. As $\varepsilon \rightarrow 0$, the diffuse interface in PF approaches the classical sharp-interface limit. Yue and co-workers extensively investigated PF methods for the modelling of interfacial dynamics in the two-phase immiscible flow of complex/non-Newtonian fluids and MCL problems²⁸⁻³⁰. Apart from interfacial dynamics, the PF model was also tested for the modelling of complex rheology of fluids in their works. It was reported that the variational framework-based PF models could easily accommodate the modelling of complex fluid behaviors. In their work on the MCL problems, Yue suggested that the mobility and capillary width are independent of each other as $\gamma \sim \varepsilon^0$ and mobility need not be compensated for the change in capillary width (ε), in contrast to the suggestions of Jacqmin (2000)³⁰. They also pointed out that a sharp-interface limit can be approached by scaling mobility with capillary width as $\gamma \sim \varepsilon^2$. Ding et al. employed PF modelling to investigate interfacial dynamics of density contrast fluids (e.g. gas and liquid)³¹. The investigation by Yue and co-workers mentioned above has mostly focused on the density-matching fluids because they observed non-convergence for the density contrast fluids. Ding suggested a scaling of mobility in the form of Peclet number (Pe) with the Cahn number (Ca) as $Pe \sim (Ca)^{-2}$ in the PF modelling of density contrast fluids. Cai and co-workers have worked extensively on the PF-based numerical modelling of the immiscible two-phase flows of gas and liquid in different interfacial flow applications^{32,33}. They implemented a PF model based on the CH-PF equation in the *OpenFOAM*[®] (called *PhaseFieldFoam*) and tested its applicability in MCL and other two-phase flow problems. They have also performed a detailed investigation on the effect of PF model parameters such as mobility, interfacial resolution, and thickness on the numerical results in the context of MCL/two-phase flow problems of gas-liquid flows, such as spreading of drops or formation of bubbles. Several suggestions made by earlier investigators regarding the tuning of the model parameters were tested by their group. They reported that the resolution of capillary width or interfacial thickness (DI) by four or higher mesh elements for $\varepsilon \leq 0.02L_c$ (where L_c is the characteristic length) would provide numerical results independent of ε . Their suggestions for the selection of PF parameters have also been implemented in the present work. In recent work, Bai et al.³⁴ conducted a numerical investigation on the droplet formation in a liquid-liquid immiscible two-phase flow in a microfluidic flow-focusing geometry using the PF method. They implemented the selection criteria for the mobility parameter suggested by Yue et al.³⁵ and examined the effect of different

orders of mobility parameters on the size and shape of the droplet formation. The simulation results were compared with similar experimental observations, and it was reported that PF mobility is a phenomenological parameter whose magnitude can be accurately decided by comparing the simulation results with experimental observations. In a recent work, Samkhaniani et al.³⁶ employed the PF model, *PhaseFieldFoam*, developed by Cai et al. earlier, to model droplet impingement dynamics on heated hydrophobic surfaces. They observed that the PF model can adequately resolve the interfacial evolution during impact dynamics. Their simulation results closely match the experimental observations reported by Guo et al.³⁷. They also reported that the wetting characteristics did not significantly affect heat transfer for the investigated range of contact angles.

It is evident from the literature that the PF methods are capable of modelling complex phenomena such as MCL problems and topological changes in two-phase immiscible and other interfacial flows. Their free energy-based modelling approach and thermodynamic consistency make them suitable for the modelling of interfacial dynamics in a wide variety of physical problems. The no-slip boundary condition, which is often challenging to implement in sharp-interface methods due to the occurrence of stress singularity, can be implemented in the PF method. However, it can also be inferred from the earlier studies that the tuning of PF model parameters is required for accurate numerical results. In the present work, PF-based computational modelling of the impingement dynamics of ferrofluid droplets is carried out on a solid substrate across a range of Weber numbers and wettability characteristics, both in the absence and presence of a magnetic field. A validation study has also been performed to establish the accuracy of the obtained numerical results. This study delves into the impact dynamics of ferrofluid droplets on heated surfaces under the influence of an applied magnetic field, shedding light on the interplay between magnetic forces, fluid flow, and heat transfer during droplet impact.

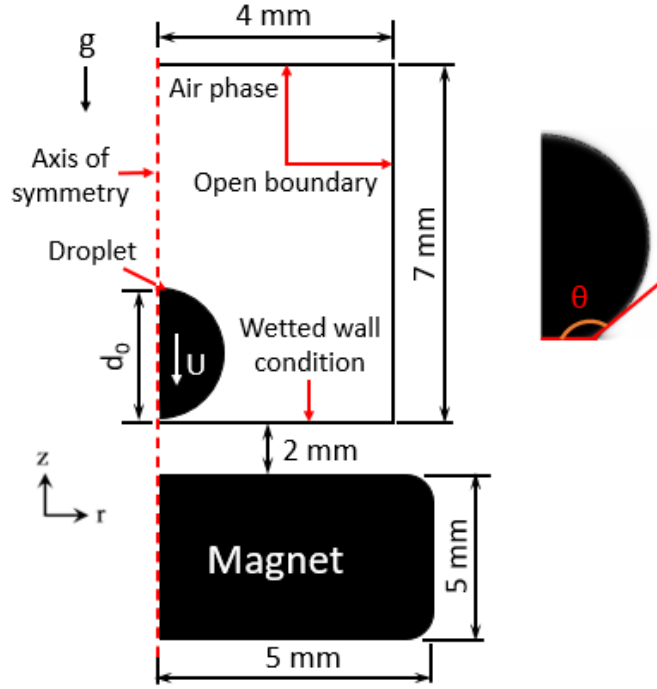


Figure 1: Schematic of the problem statement with dimensions and boundary conditions

2. Computational Modelling and Methodology

The impingement dynamics of ferrofluid droplets are modelled on a smooth solid heated substrate in the presence of an externally applied magnetic field (MF) at different Weber numbers (We) and wetting conditions (equilibrium contact angles, θ_e), spanning both hydrophilic and hydrophobic regimes. The applied magnetic field is produced by simulating a finite-size permanent magnet. The Weber number ($We = \rho U^2 d_0 / \sigma$), representing the ratio of kinetic to surface energy, assesses the relative influence of inertial and surface tension forces during morphological evolution. At high We , inertial forces dominate, leading to droplet breakup and wave formation, while at low We , surface tension prevails, resulting in stable droplet formation. The Reynolds number ($Re = \rho U d_0 / \mu$), the ratio of inertial to viscous forces, and the magnetic Bond number ($Bo_m = B^2 d_0 / \mu_0 \sigma$), the ratio of magnetic to surface tension forces, is employed to analyze the effects of the relative importance of different forces during droplet dynamics. Here, ρ , μ , and σ represent the density, viscosity, and surface tension of fluids, respectively; U is the initial droplet impact velocity; d_0 is the initial droplet diameter; and B is the applied magnetic field intensity in Tesla. The magnitude of magnetic permeability, $\mu_0 = 4\pi \times 10^{-7} \text{ N/A}^2$.

A single set of continuity, momentum and energy equations is solved numerically to simulate the thermal transport characteristics of the impinging droplet. The multiphase flow is modelled

as incompressible, immiscible, and non-boiling flow, and ferrofluid (*ff*) is modelled as a pseudo-single-phase Newtonian liquid with magnetic characteristics. The time scale of the impinging dynamics is of the order $\sim O(10^{-3} \text{ s})$, which is much larger than the relaxation time scale for material magnetization $\sim O(10^{-5} \text{ s})$. Therefore, it is assumed that the magnetization of MNPs in suspension will remain aligned with the direction of applied MF, and thus, angular momentum considerations have been neglected in the momentum equation. The interfacial evolution of impinging droplet dynamics (spreading, receding and bounce-off phases) is simulated using the Phase-field (PF) formulation, a diffuse interface-based methodology for modelling interfacial multiphase flows²⁷. In the PF method, a scalar ordered parameter called the phase-field parameter (ϕ) is used to differentiate between the two phases. It is assigned two distinct values (-1 for air and +1 for ferrofluid) in the bulk of the material phases, with a rapid but smooth transition in the interfacial regions.

An axis-symmetric schematic of the problem statement with relevant dimensions and boundary conditions is shown in Figure 1. This same setup is modelled and simulated to study the droplets' impingement dynamics and thermal transport characteristics in the absence and presence of a magnetic field. A cylindrical permanent magnet of dimensions 5 mm (thickness) \times 10 mm (diameter) is numerically modelled using the Gauss divergence equation (Eq. 1) to simulate the applied MF. The magnet is placed 2 mm below the air domain, as shown in Figure 1. An air domain is defined around all the objects to simulate the magnetic field. The following equations with specified boundary conditions are numerically solved to create the applied MF,

$$\nabla \cdot \mathbf{B} = 0; \mathbf{B} = \mu_0(\mathbf{H} + \mathbf{M}) \quad (1)$$

where \mathbf{B} , \mathbf{H} and \mathbf{M} represent magnetic induction (or flux density, in Tesla [T]), magnetic field (A/m) and magnetization (A/m), respectively. The above equations are subjected to magnetic insulation boundary conditions, $n \cdot \mathbf{B} = 0$ at the outer domain walls (n represents the normal unit vector at the boundary)⁹. The magnetic characteristics (magnetization, \mathbf{M}) of ferrofluid droplets are defined using the Langevin function^{13,38} as,

$$\mathbf{M} = M_S L(\alpha) \frac{\mathbf{H}}{|\mathbf{H}|}; L(\alpha) = \coth(\alpha) - \left(\frac{1}{\alpha}\right); \alpha = \frac{\mu_0 M_d H d_h^3}{6k_B T} \quad (2)$$

The Langevin function (Eq. 2) accurately depicts the non-linear magnetization characteristics shown by ferrofluids¹³. Here, $L(\alpha)$ denotes the Langevin function, with α being the ratio of magnetic energy to thermal energy. The equation clearly indicates that the magnetization (\mathbf{M})

of ferrofluids is influenced by various factors, including the fluid temperature (T), the size (d_h) and concentration (ϕ) of the magnetic nanoparticles (MNPs), the material's domain magnetization (M_d), and the applied magnetic field (H). Furthermore, the saturation magnetization (M_s) of ferrofluids is determined by the domain magnetization (M_d) and the volume fraction (ϕ), following the relation, $M_s = \phi M_d$. The magnetic body force (f_k) induced in ferrofluid in the presence of a magnetic field is defined as follows,

$$f_k = \mu_o(M \cdot \nabla)H \quad (3)$$

The induced magnetic force can be varied either by changing the gradient of the applied magnetic field or by magnetization (M_s) of ferrofluids, as seen in Eq. 3.

The transient multiphase flow phenomena and the interfacial evolution are simulated using continuity equation (Eq. 4), Navier Stokes (N-S) equations (Eq. 5), and Cahn-Hilliard Phase-field (CH PF) equations (Eq. 7). The thermal transport between substrate and droplet is modelled using the energy equation (Eq. 6). The solved continuity, momentum (N-S) and energy equations are as follows,

$$\nabla \cdot V = 0 \quad (4)$$

$$\frac{\partial V}{\partial t} + \rho(V \cdot \nabla)V = -\nabla P + \mu \nabla^2 V + f_g + f_{ST} + f_m \quad (5)$$

$$\frac{\partial T}{\partial t} + V \cdot \nabla T = \left(\frac{k}{\rho C_p} \right) \nabla^2 T \quad (6)$$

Where V and P are velocity (in vector form) and pressure terms, respectively. The f_g , f_{ST} and f_m terms in momentum equations represent gravity, surface tension and magnetic forces, respectively, which are defined in subsequent sections. The f_g term is defined as the product of fluid density and gravitational constant, g .

The above equations are subject to the following boundary conditions. The no-slip ($V = 0$) boundary condition is defined for the bottom surface, and zero-gauge pressure ($P = 0$) is defined for the side and top walls. A uniform and constant wall temperature ($T = 60^\circ\text{C}$) boundary condition is specified on the bottom wall of the domain. The outflow boundary ($n \cdot q'' = 0$, where q'' is heat flux defined as $q'' = -k \nabla T$) condition is defined for the top and side walls of the domain shown in Figure 1. The initial conditions for velocity and temperature are $V = 0$ and $T = 20^\circ\text{C}$.

The Cahn-Hilliard Phase-field (CH PF) equation, used to model interfacial dynamics, is a fourth-order convection-diffusion equation in phase field variables, ϕ

$$\frac{\partial \phi}{\partial t} + \mathbf{V} \cdot \nabla \phi = \nabla \cdot \frac{\gamma \lambda}{\varepsilon^2} \nabla \Psi; \Psi = -\nabla \cdot \varepsilon^2 \nabla \phi + (\phi^2 - 1)\phi \quad (7)$$

Where \mathbf{V} is fluid velocity and γ , λ , and ε are called the mobility, mixing energy density and interface thickness parameters, respectively. Parameter ϕ takes a value of -1 and +1 in the bulk of the binary fluid system (gas and liquid in the present case) with a rapid but smooth transition in the interfacial region. The interface between two fluids is defined by $\phi = 0$ contours. The phase-field mobility (γ) is another critical parameter defined in the CH-PF equation. It governs the time scales of advection and diffusion terms of the phase-field parameter (ϕ) and affects an out-of-equilibrium interface's time scale of relaxation³⁴. A scaling relationship between the mobility and interface thickness parameters as $\gamma \sim \varepsilon^2$ is suggested by Jacqmin²⁷ for a stable evolution of the interface, and this is also implemented in the PF formulation on the COMSOL Multiphysics® (V 5.3a) platform. In the present simulations, γ is defined as $\gamma = \chi \varepsilon^2$, and its magnitude is controlled through a mobility tuning parameter (χ).

The variable ψ (called phase-field help variable) is used to divide the fourth-order CH PF equation into two second-order PDEs, and, ε , as its name suggests, it controls the thickness of the interface. The relationship between surface/interfacial tension (σ), λ and ε is given by

$$\sigma = \frac{2\sqrt{2} \lambda}{3 \varepsilon} \quad (8)$$

The chemical potential (G) of the two-fluid system and surface tension force (f_{ST}) are related as,

$$G = \frac{\lambda \Psi}{\varepsilon^2}; f_{ST} = G \nabla \phi \quad (9)$$

The volume fraction of individual fluids and the thermophysical properties of the two-phase mixture (air and liquid) used are defined in terms of ϕ as,

$$Vf_1 = \frac{1 - \phi}{2}; Vf_2 = \frac{1 + \phi}{2} \quad (10)$$

$$\rho_{TP} = \rho_{air} Vf_1 + \rho_{ff} Vf_2; \mu_{TP} = \mu_{air} Vf_1 + \mu_{ff} Vf_2 \quad (11)$$

$$k_{TP} = k_{air} Vf_1 + k_{ff} Vf_2; C_{p_{TP}} = C_{p_{air}} Vf_1 + C_{p_{ff}} Vf_2$$

Where Vf_1 and Vf_2 represent the volume fraction of gas and liquid phases. The subscripts *air*, *ff* and *TP* are used for the gas (air), ferrofluid, and two-phase mixture phases. The symbols ρ , μ , k , and C_p represent density, viscosity, thermal conductivity and specific heat (thermophysical properties) of individual and mixture phases. The following properties of the fluids are used in simulations:

Table 1: Fluid properties used in the computational modelling

Material	Density (ρ , kg/m ³)	Viscosity (μ , Pa-s) $\times 10^{-5}$	Thermal Conductivity (k , W/m-K)	Specific heat (C_p , J/kg-K)	Surface tension (σ , N/m)
Air	1.3	1.5	0.026	1000	-
Water	998	90	0.60	4180	0.070
Ferrofluid	1018	91	0.60	4090	0.035

3. Results and discussion

3.1 Validation

Firstly, a validation study is performed to assess the accuracy of computational modelling of such multiphase flow phenomena using Phase-field formulation implemented on the COMSOL Multiphysics platform. The experimental work of Guo et al. ³⁷ and the computational modelling of the same work by Samkhaniani et al. ³⁶ are considered for validation. They implemented *PhaseFieldFoam* on the OpenFOAM platform using their numerical modelling approach and investigated the thermal transport characteristics of impinging aqueous droplets on heated hydrophobic/superhydrophobic substrates. Figure 2(a) presents a comparison of the present work with Guo and Samkhaniani's works for temporal interfacial evolution of the droplet after impact for Weber number (We) = 20, $d_0 = 2.3$ mm and contact angle (θ_e) of 120°. A quantitative comparison of the normalized maximum spreading diameter called the spreading parameter, $\beta(t) = d(t)/d_0$, is also presented in Figure 2(b). As seen in the referred figures, the present simulation results are in good agreement with the previous works. The maximum spreading diameter during advancing and receding phases closely matches experimental and numerical observations reported in earlier studies. This validation exercise provided the necessary confidence in the present modelling approach. The present simulations are carried out at Cahn number (Cn) = 0.01, resulting in a maximum mesh element size (h_{max}) of 2.3×10^{-5} m or 23 μ m (Cn is defined as the ratio of maximum mesh element size to initial droplet diameter, $Cn = h_{max}/d_0$). The $Cn = 0.01$ provides four mesh elements in the interfacial regions for the resolution of the interfacial thickness (defined by contours of $-0.9 < \phi < 0.9$), which is generally considered sufficient to resolve the interfacial region ^{33,34}. This same mesh size (corresponding to $Cn = 0.01$) is used for all the studied cases in the present work. The variation of PF parameter ϕ in the range -0.9 to $+0.9$ in the interfacial region represents 98.5% of the

interfacial stress and is generally considered as the thickness of the interface^{39,40}. The value of mobility tuning parameter (χ) is kept 1 in all the simulations.

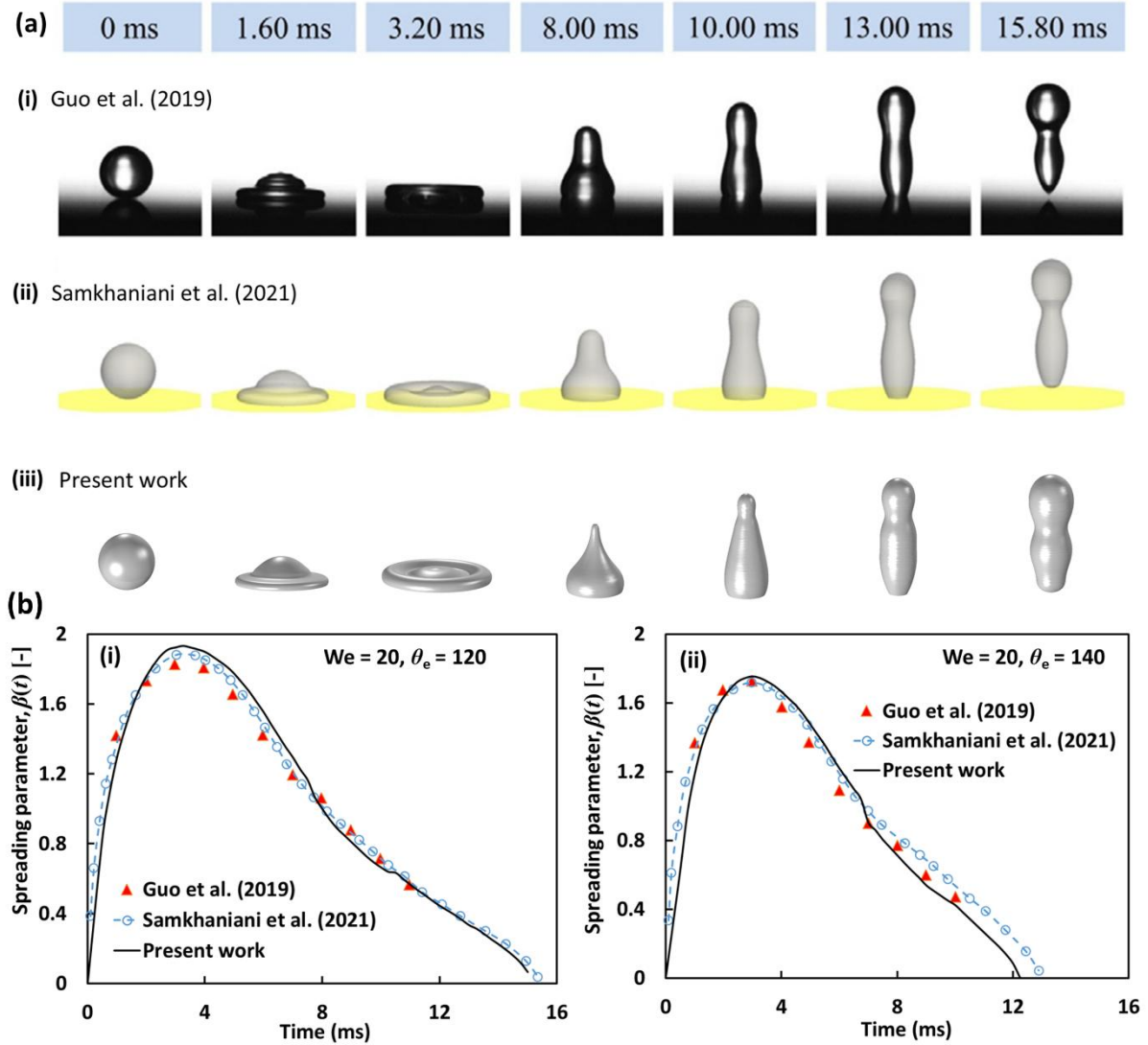


Figure 2: (a) Comparison of present simulations results for temporal interfacial evolution of the impinging droplet with earlier works for $We = 20$ and $\theta_e = 120^\circ$ (b) Comparison of results for normalized spreading parameter, $\beta(t) = d(t)/d_0$ with previous studies at $We = 20$ and (i) $\theta_e = 120^\circ$ (ii) $\theta_e = 140^\circ$.

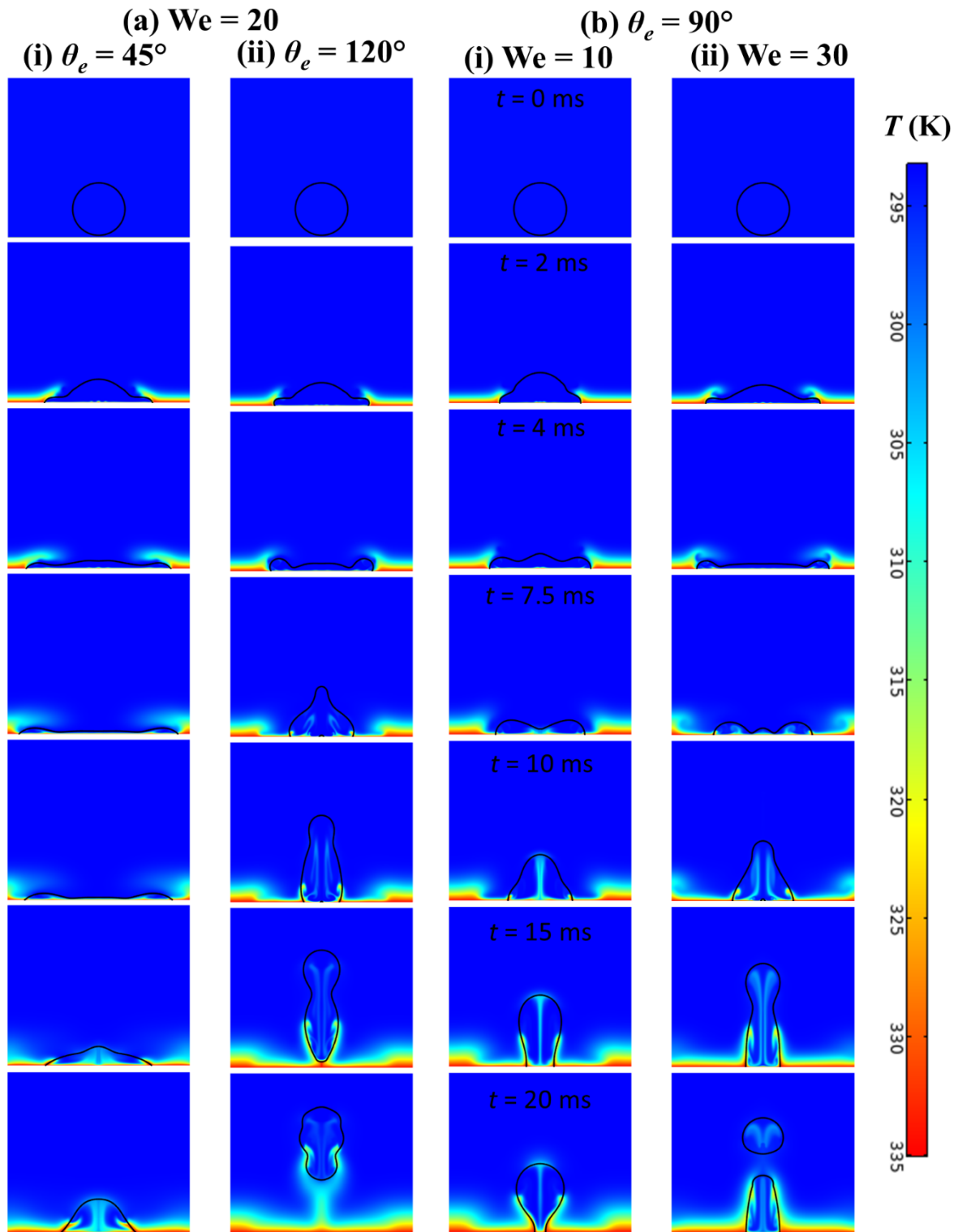


Figure 3: A comparison of morphological evolutions (advancing and receding phases) of the droplet after impact at (a) $We = 20$ for (i) $\theta_e = 45^\circ$ and (ii) $\theta_e = 120^\circ$ and at (b) $\theta_e = 90^\circ$ for (i) $We = 10$ and (ii) $We = 30$ cases.

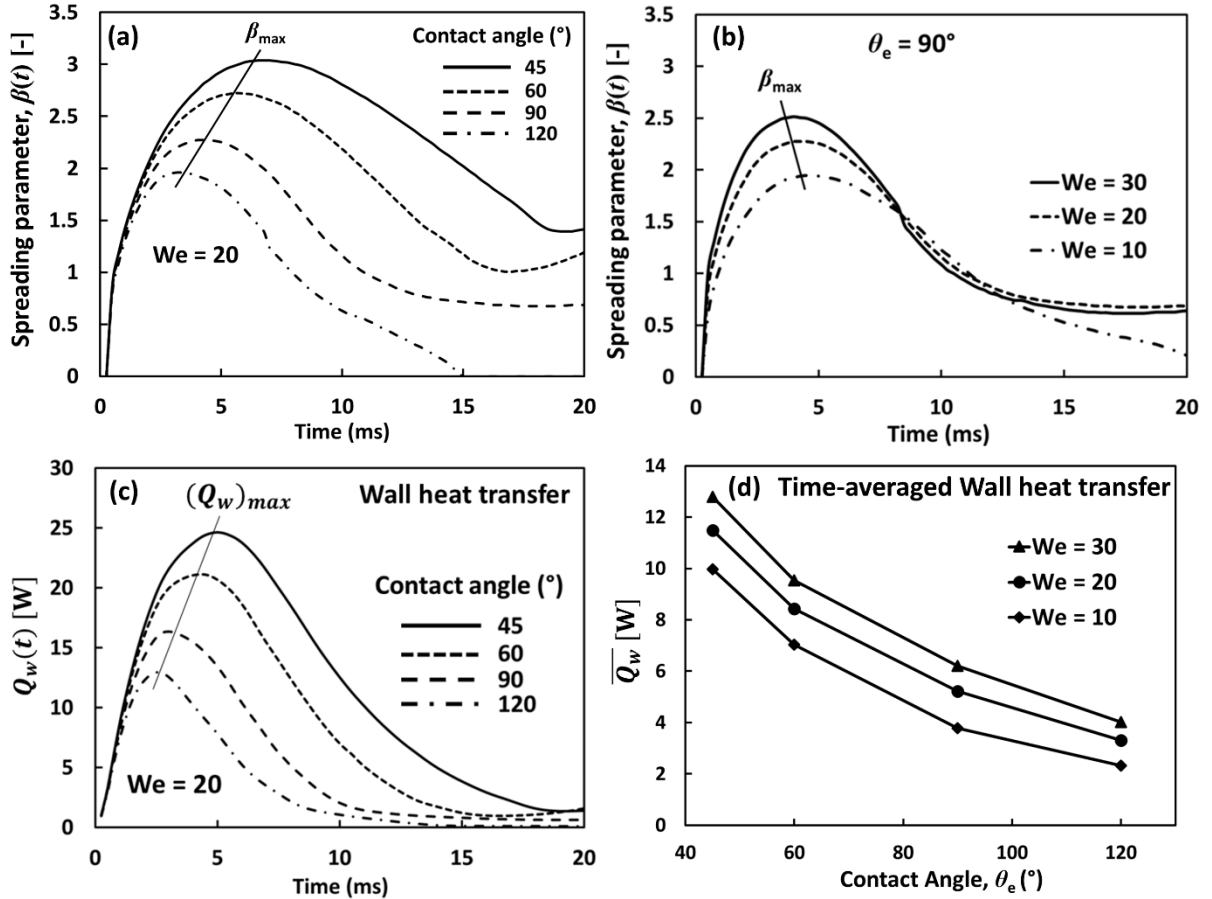


Figure 4: Spreading parameter, $\beta(t)$ during interfacial evolution for (a) different wetting conditions (contact angles) at $We = 20$ and (b) different Weber numbers at $\theta_e = 90^\circ$ (c) associated temporal variation of total wall heat exchanged with the evolution of the impinging droplet for different contact angles at $We = 20$ (d) Time-averaged (20 ms) wall heat transfer for different Weber numbers and contact angles.

3.2 Aqueous droplets (No-field cases)

The validation study is extended to investigate the effect of inertia force (through Weber number) and wetting characteristics (equilibrium contact angle, θ_e) on the spreading parameter, β , and associated heat transfer characteristics. The Weber number is varied in the range of 10 to 30, and the contact angle in the range of 45° to 120° , covering both hydrophilic and hydrophobic regimes. The corresponding impact velocity Reynolds number is in the range of 1022 – 3066. Figure 3(a, b) shows a comparison of the morphological evolution of the droplet after impact and associated temperature distribution for hydrophilic ($\theta_e = 45^\circ$) and hydrophobic ($\theta_e = 120^\circ$) cases at $We = 20$. A distinction between advancing and receding phases can be seen clearly in both cases. As seen from the figure, no bounce-off is observed during the receding phase for the hydrophilic surface. The initial position ($t = 0$) of the droplet can also be seen in

the snapshots of Figure 3. The maximum spreading diameter and wall heat transfer are also highest for $\theta_e = 45^\circ$ among all investigated cases, as seen in Figure 3(c, d).

Across the investigated Weber number range, both inertia and surface tension significantly influenced droplet impact dynamics. The inertia drives the initial spreading, converting kinetic energy to surface energy as the contact area increases. Hydrophilic surfaces promoted spreading due to strong fluid-surface attraction, while hydrophobic surfaces hindered it. As the droplet reached maximum spread, inertial effects diminished, and capillary and viscous forces became dominant. On hydrophilic surfaces, strong surface attraction resisted retraction, leading to a slower receding phase, a larger final contact area, and, consequently, higher contact time. Conversely, weak attraction on hydrophobic surfaces resulted in rapid retraction and recoil, often with complete or partial rebound. This difference in spreading and receding behavior significantly impacted heat transfer. The hydrophilic surface ($\theta_e = 45^\circ$) exhibited the highest contact time and, consequently, the highest heat transfer (Figure 3(d) and 4(d)). Heat transfer for the $\theta_e = 45^\circ$ cases was approximately two to three times greater than the hydrophobic ($\theta_e = 120^\circ$) cases, depending on the Weber number. Figure 4(a-c) illustrates the effect of the Weber number on spreading and receding. The maximum droplet deformation occurs around 3 to 6 ms, depending on the surface wettability and Weber number. The maximum spreading diameter increased with the Weber number, as expected, due to higher impact inertia. Consequently, the highest heat transfer was observed at $We = 30$, approximately 30% higher than the $We = 10$ case for $\theta_e = 45^\circ$. Figure 4(d) summarizes the overall heat transfer for all cases. The total wall heat transfer was computed for $We = 10 - 30$ and $\theta_e = 45^\circ - 120^\circ$. The droplet impact time scale is on the order of 10 – 20 ms (Figures 2, 3 and 4), and the time-averaged heat transfer (Figure 4(d)) is computed by averaging transient heat transfer data over 20 ms time scale. As expected, the maximum heat transfer occurred at the highest Weber number ($We = 30$) and lowest contact angle ($\theta_e = 45^\circ$). A high Weber number signifies high droplet inertia at a given surface tension. Combined with the hydrophilic regime ($\theta_e = 45^\circ$), which maximizes interaction time with the substrate (~ 20 ms for a complete spreading and receding cycle, as seen in Figure 3(a)), this resulted in the highest overall heat transfer. Several correlations have already been proposed to predict the maximum spreading diameter and heat transfer rate during droplet impingement dynamics.

3.3 Effect of magnetic field

Finally, the study investigated the influence of a magnetic field on the impingement dynamics of ferrofluid droplets. The magnet, positioned 2 mm below the fluid domain's bottom wall (Figure 1), generated a spatially varying magnetic field with a maximum intensity (B_{\max}) of 0.23 T. The corresponding magnetic Bond number $(Bo_m)_{\max}$ is 2768. More details on modelling and validation of the magnetic field produced by the considered finite-sized permanent magnet are presented in our previous works^{8,9,13}. This field induced a substantial magnetic body force (order of magnitude $\sim 10^8$) within the fluid domain, exceeding the droplet's maximum inertial force ($\sim O(10^6)$) by two orders of magnitude, thus significantly altering the impingement dynamics, particularly on hydrophobic surfaces.

A qualitative and quantitative comparison of maximum spreading diameter, temperature distribution, and average wall heat transfer with and without the magnetic field is presented in Figures 5 and 6. Without the magnetic field, droplets on hydrophobic/superhydrophobic surfaces ($\theta_e \geq 120^\circ$) exhibited a pronounced rebound (Figure 5(a) and Figure 6, $We = 20$), detaching from the surface at approximately 15 ms. However, the application of the magnetic field effectively eliminated this rebound. Furthermore, the magnetic field significantly increased the maximum spreading diameter ($\sim 25\%$) and the droplet's contact time with the heated substrate (Figure 6). Consequently, heat transfer is enhanced substantially compared to identical scenarios without the magnetic field. These results demonstrate the significant potential of magnetic forces in manipulating droplet behavior and improving heat transfer during impingement. Specifically, the time-averaged heat flux with the magnetic field was $\sim 66\%$ higher than the no-field case, as seen in Figure 6.

The effect of Weber number and contact angle on spreading dynamics and heat transfer characteristics is also examined in the presence of the magnetic field. Figure 7(a, b) compares morphological evolution and associated temperature distribution at wetting conditions of 45° and 120° for $We = 30$ cases, and Figure 7(c) shows the same for $We = 20$ and $\theta_e = 90^\circ$ case. The variation of $\beta(t)$ for all contact angles at $We = 20$ and for all Weber numbers at $\theta_e = 90^\circ$ is presented in Figure 8(a, b). As seen in the image snapshots of Figure 7(a, b), the contact angle has a significant influence on the morphological evolution of the droplet, even in the presence of the magnetic field (which induces a body force of two orders of magnitude higher than the inertia force). This is further evident from the plots of $\beta(t)$ presented in Figure 8(a). The maximum spreading parameter is again higher for the hydrophilic case ($\theta_e = 45^\circ$) compared to all other cases, as seen from the plots. Maximum spreading is aided by the magnetic force,

which acts in the same direction as the inertia force. This results in a higher contact time for the droplet, thereby enhancing the overall heat transfer, as seen in Figure 8(c). The presence of a magnetic field significantly improves the heat transfer rate, even for hydrophilic cases.

Weber number, $We = 20$, Contact angle, $\theta_e = 120^\circ$

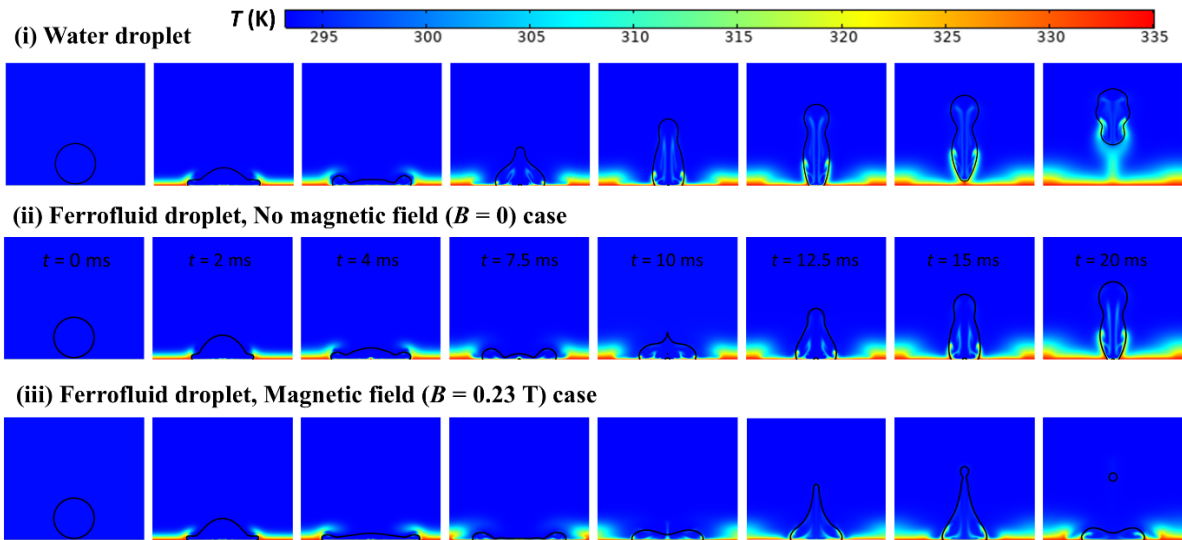


Figure 5: A comparison of droplet impingement dynamics at $We = 20$, $\theta_e = 120^\circ$) for (i) water droplet (ii) No-magnetic field cases, $B = 0$ (spreading, receding and rebounding phases can be seen), (iii) Magnetic field ($B_{max} = 0.23$ T) case, again spreading and receding phases can be seen while rebounding phases have been suppressed by the magnetic force. The associated temperature distribution and the initial position of the droplet can also be seen in both cases.

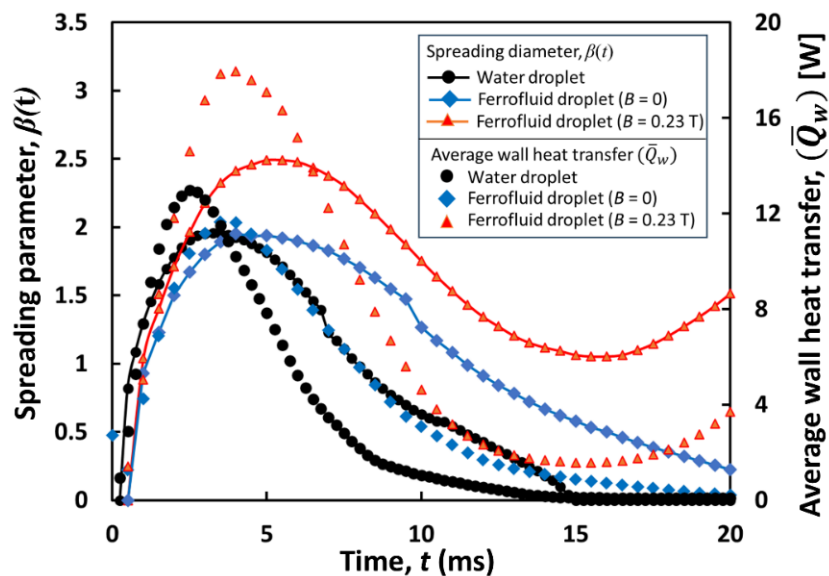


Figure 6: Quantitative analysis of $\beta(t)$ and average wall heat transfer (\bar{Q}_w) for the three cases shown in Figure 5. As seen from the plots, higher heat transfer occurs in the magnetic field case as droplet bounce-off is suppressed by the magnetic force, resulting in higher contact time between the droplet and substrate.

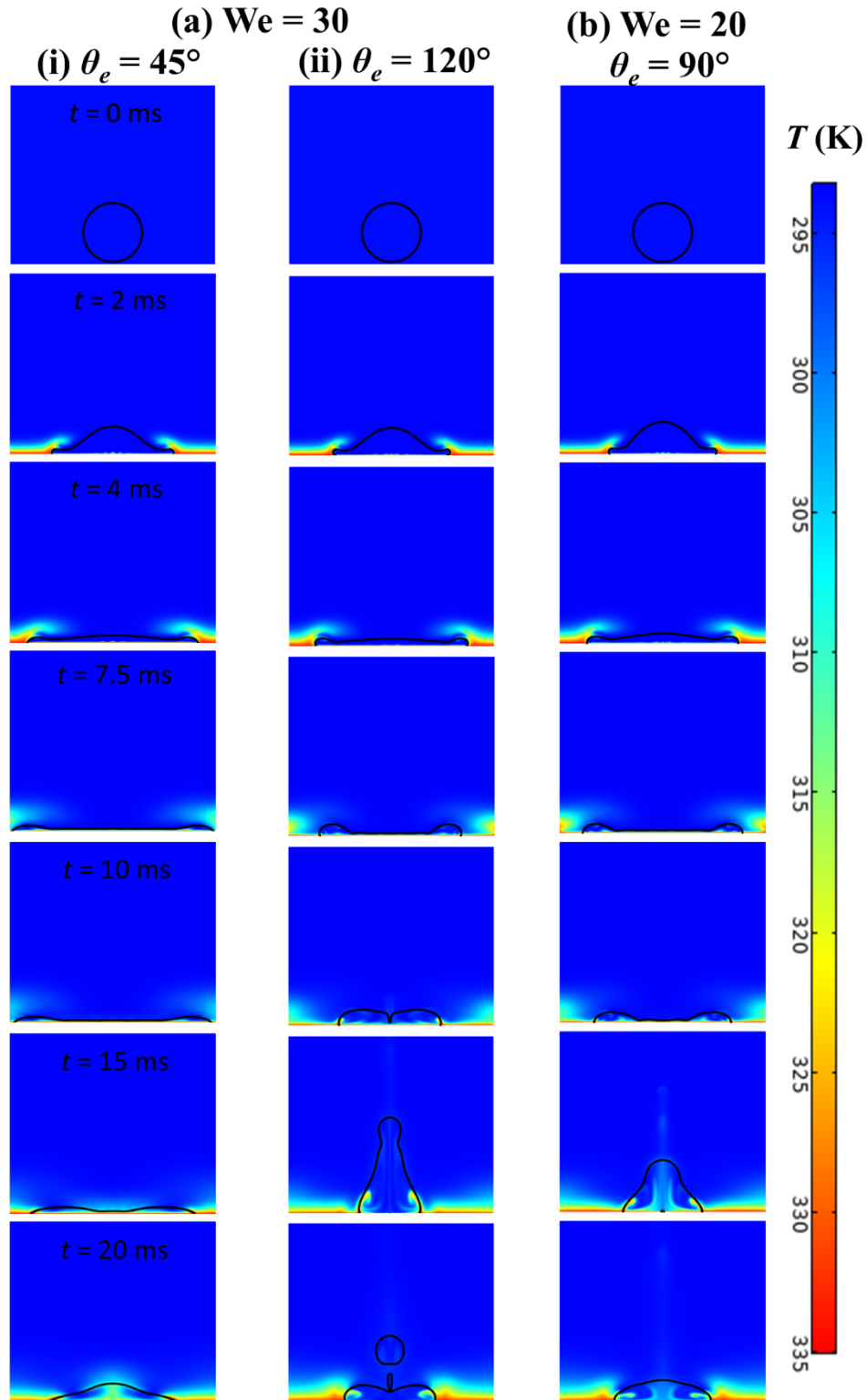


Figure 7: A comparison of morphological evolution (advancing and receding phases) of the droplet after impact at (a) $We = 30$ for (i) $\theta_e = 45^\circ$ and (ii) $\theta_e = 120^\circ$ in the presence of the magnetic field. (For $We = 20$, $\theta_e = 120^\circ$ case snapshots, refer to Figure 5) (c) Evolution of the droplet after impact at $We = 20$ for $\theta_e = 90^\circ$ cases in the presence of the magnetic field.

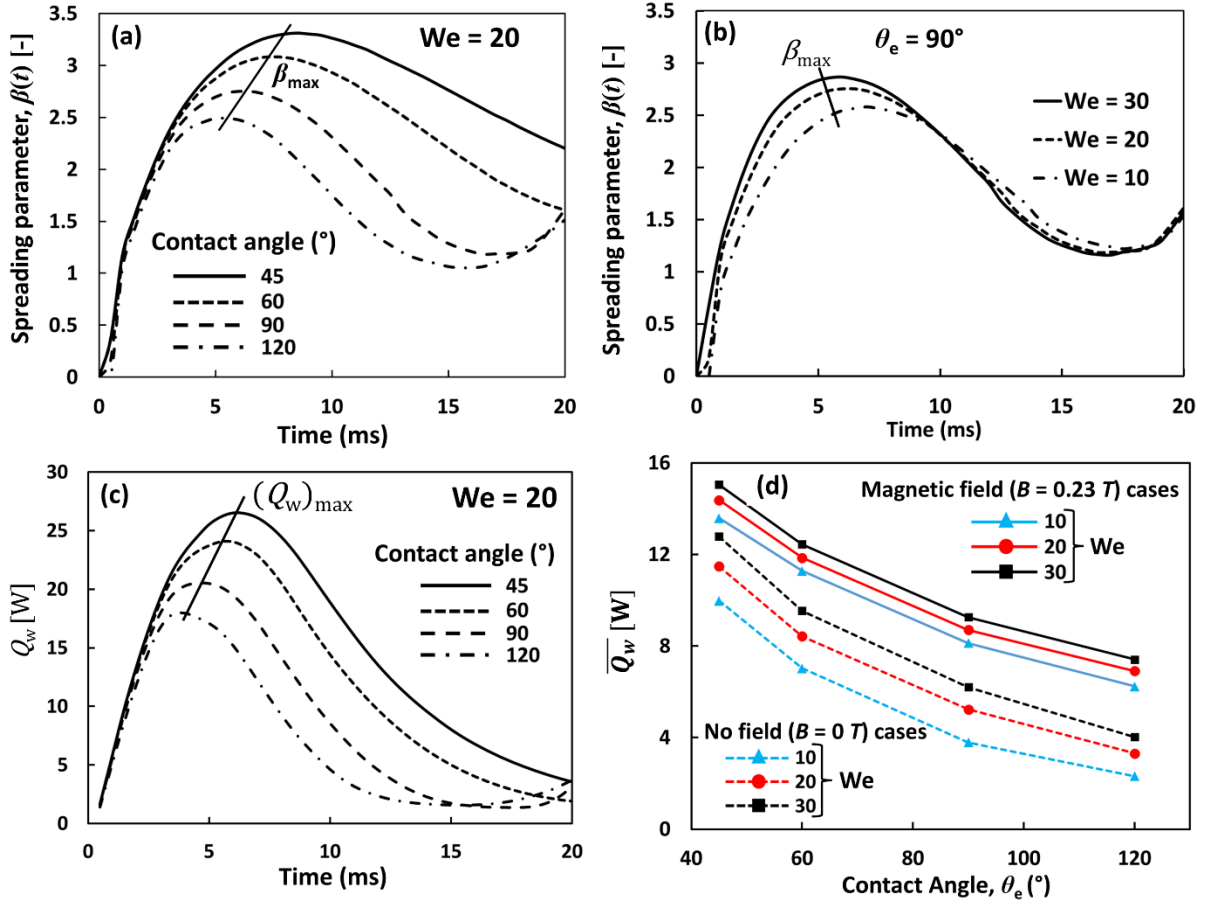


Figure 8: Comparison of plots of the spreading parameter, $\beta(t)$, during evolution for (a) different wetting conditions (contact angles) at $We = 20$ (b) at $\theta_e = 90^\circ$ for different Weber numbers (c) Associated temporal variation of wall heat transfer (Q_w) with the evolution of the impinging droplet for different contact angles at $We = 20$. (d) Time-averaged (20 ms) wall heat transfer ($\overline{Q_w}$) for different Weber numbers and contact angles.

Figure 7(c), in conjunction with 8(b), illustrates the effect of Weber number on spreading dynamics for the contact angle (θ_e) of 90° . Notably, varying the Weber number has minimal impact on impingement dynamics in the presence of a magnetic field. This contrasts sharply with cases without a magnetic field, where inertia plays a dominant role during the spreading phase. The induced magnetic force, approximately two orders of magnitude greater than the inertia force, effectively negates the influence of inertia and capillary forces during the spreading and receding phases. Similar observations have also been reported by Ahmed et al.¹⁷, where they observed that while the magnitude of maximum spreading changed with applied field intensity, the maximum spreading always occurred at around 6.5 ms after impact, similar to the present case. This dominance is further evident in the time-averaged (20 ms) heat transfer data presented in Figure 8(d) for all the investigated cases. Without a magnetic field,

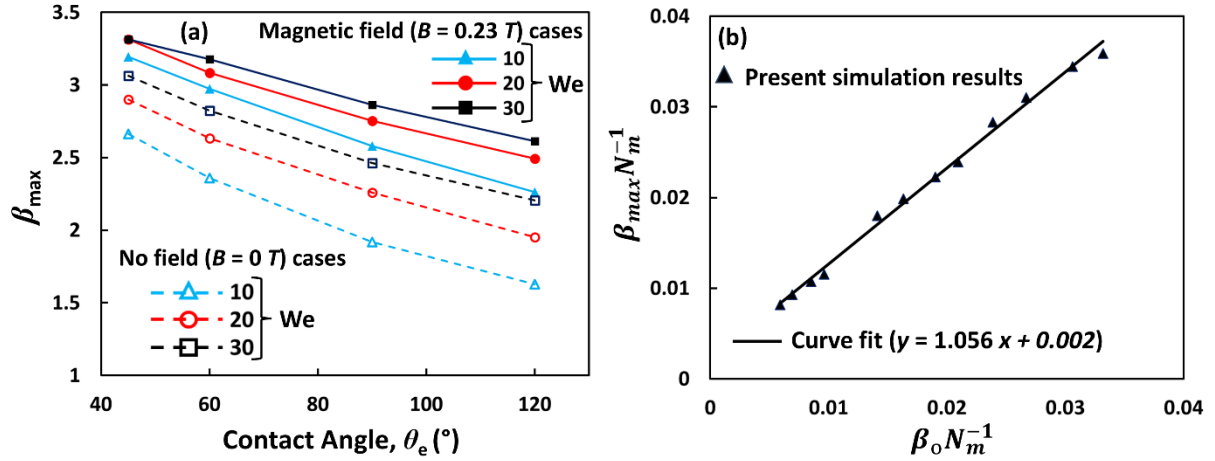


Figure 9: (a) Comparison of maximum spreading parameter (β_{\max}) for both magnetic and non-magnetic field cases (b) A general correlation developed based on previous scaling analysis for the prediction of β_{\max} for magnetic field cases based on maximum spreading in no-field (β_0) cases.

the expected trends are observed: heat transfer increases with increasing inertia force (Weber number) and decreases with increasing contact angle (as the surface becomes more hydrophobic). However, with the magnetic field applied, the differences between cases diminish significantly, indicating that the magnetic field's influence overshadows the contributions of inertia and capillary forces. A maximum enhancement of about 170% for the $We = 10$ and $(\theta_e) = 120^\circ$ case and a minimum enhancement of $\sim 17\%$ for the $We = 30$ and $(\theta_e) = 45^\circ$ case are observed in the presence of the magnetic field among all the investigated cases. The enhancement in heat transfer decreases with increasing Weber number, as seen in Figure 8(d). A general-purpose correlation is developed to predict the maximum spreading diameter (β_{\max}) in an applied non-uniform magnetic field (which can give rise to Kelvin body force). In the present work, both Weber number and contact angle are changed while other parameters are kept constant. The Weber number is changed by changing the inertia force, while surface tension forces are kept constant. The present findings align closely with those reported by Benter et al.²³ from their analogous experimental study. Specifically, they observed an average heat transfer rate of ~ 14 watts under magnetic field conditions, at $We = 60$ and $\theta_e = 45^\circ$, which corroborates the heat transfer magnitudes obtained in this current investigation, thereby lending further credence to the reliability and accuracy of the computational methodology employed herein. Figure 9(a) presents a comparison of the maximum spreading parameter (β_{\max}) for both magnetic field and non-magnetic field cases of ferrofluid. The maximum change in β_{\max} is observed for $We = 10$ cases, and the effect of the applied magnetic

field is increasingly overcome by the inertial forces, as the Weber number increases to 30. The maximum observed change is around 40% at $We = 10$, $\theta_c = 120^\circ$. This indicates that a tuning of magnetic force is required to get the desired effect at higher Weber numbers.

Finally, a general relationship is proposed to predict the maximum spreading (β_{\max}) in the presence of a magnetic field, based on scaling arguments presented by Li et al.²¹ and Huang et al.²². It is known that the initial droplet spreading is driven by an increase in the local pressure at the centre of the droplet upon impact. This increase in pressure causes droplets to spread. As droplets spread, capillary and viscous forces progressively increase and finally overcome inertial forces at maximum spreading. In the pressure-driven stage, the time scale of droplet spread is given by $t \sim do/U$. When a magnetic field is applied, the induced magnetic force, which is attractive in nature and oriented in the same direction as the inertia forces at the time of impact, makes the pressure gradient stronger. They argued that the induced magnetic force aids inertia force during the droplet spreading phase, and the motion of the droplet is governed by magnetic force. Through scaling arguments, Li et al., proposed a non-dimensional magnetic parameter, $N_m \sim \mu_o \rho U^2 / B^2$, defined as the ratio of inertia to magnetic force to describe the motion of the droplet in the pressure-driven regime. Also, by assuming the complete conversion of kinetic energy to surface energy and dissipation into thermal energy at maximum spreading, their scaling analysis relates maximum spreading in the presence of a magnetic field with magnetic parameter (N_m) as $\beta_{\max} \sim N_m$. Based on their analysis, Li et al proposed a correlation to predict maximum spreading for the magnetic field cases by relating it to maximum spreading with no magnetic field case at the same Weber number and N_m , as $\beta_{\max} \sim f(\beta_o N_m^{-1})$, where β_o represents maximum spreading for no field cases. The proposed functional form for the correlation is $\beta_{\max} N_m^{-1} = P / (1 + AP)$ where $P = \beta_o N_m^{-1}$ and A is the curve fitting coefficient. By relating β_{\max} with β_o , they accounted for viscous and capillary effects in spreading dynamics. Huang et al. used a similar scaling approach to relate β_{\max} with N_m as $\beta_{\max} \sim N_m^{-1/2}$. They also proposed a similar correlation to Li et al. for the prediction of the maximum spreading parameter in the presence of a magnetic field.

Based on earlier scaling analysis, a general relationship is also being proposed in the present work to predict the maximum spreading parameter in the presence of the magnetic field. Figure 9(b) shows a curve fit to the present data. A linear function of the form, $y = a x + b$, has been used to fit the outcome of the present work. Here, $y = \beta_{\max} N_m^{-1}$ and $x = \beta_o N_m^{-1}$ represent the same physical parameters as in previous works. a and b are the curve slope and y-axis intercept, respectively, with values of 1.056 and 0.002 for the present work. To validate this functional

form, the experimental results of Banthar et al.²³ have been used. The β_{\max} value for the heated substrate, magnetic field case, is around 2.50 in their case, and the proposed correlation predicts it to be around 2.45, which is close to the actual experimental values. This further reinforces confidence in the proposed correlation.

In summary, when the induced magnetic force is significantly stronger than inertia, capillary, and viscous forces, it becomes the primary driver of the impingement dynamics and associated heat transfer characteristics.

Summary and Conclusions:

This study investigated the thermal transport characteristics of ferrofluid droplets impinging on a heated surface under the influence of a magnetic field. The magnetic field produced by a finite-size permanent magnet is simulated using Maxwell's equations. A single set of mass, momentum, and energy equations, coupled with a phase-field formulation, modelled the droplet impingement dynamics and interfacial evolution on both hydrophilic and hydrophobic surfaces. In the absence of a magnetic field, surface wettability significantly affected the spreading and receding phases, with hydrophilic surfaces promoting spreading and hydrophobic surfaces facilitating recoil. However, the application of a magnetic field, inducing an attractive magnetic body force due to the ferrofluid's super-paramagnetism, substantially increased the maximum spreading diameter on both surface types and suppressed droplet rebound on hydrophobic surfaces. This demonstrates the magnetic force's significant influence on spreading dynamics, counteracting the inertia and capillary forces. Consequently, a maximum heat transfer enhancement of $\sim 75\%$ was observed with the magnetic field compared to the no-field case at a Weber number of 30 and a contact angle of 120° . This enhancement is attributed to the increased spreading diameter and suppressed rebound, resulting in a larger contact area and more efficient heat exchange between the droplet and the heated surface.

The ability to manipulate droplet behavior and heat transfer using external magnetic fields opens up possibilities for dynamic control of thermal management systems, enabling on-demand adjustment of cooling rates. This could be particularly useful in applications with fluctuating heat loads, for example, in designing a thermal switch.

ACKNOWLEDGEMENT

The author would like to thank UPES for providing the required facilities and resources to conduct this work. The author would also like to thank Dr Debartha Chatterjee, IIT Kanpur, for his support in performing computer simulations and Dr Ankush Jaiswal, IIT Hyderabad, for reviewing and providing valuable suggestions for this work. This research did not receive any specific grant from funding agencies in the public, commercial, or not-for-profit sectors.

AUTHOR DECLARATIONS

Conflict of Interest

The author has no conflict of interest to disclose.

Data Availability

The data that support the findings of this study are available within the article.

References

- ¹ J. Kim, "Spray cooling heat transfer: The state of the art," *Int J Heat Fluid Flow* **28**(4), 753–767 (2007).
- ² G. Liang, and I. Mudawar, "Review of spray cooling – Part 1: Single-phase and nucleate boiling regimes, and critical heat flux," *Int J Heat Mass Transf* **115**, 1174–1205 (2017).
- ³ A.K. Jaiswal, and S. Khandekar, "Transient heat transfer during consecutive impact of two droplets on a heated substrate," *International Journal of Thermal Sciences* **193**, 108546 (2023).
- ⁴ A.K. Jaiswal, and S. Khandekar, "Drop-on-Drop Impact Dynamics on a Superhydrophobic Surface," *Langmuir* **37**(43), 12629–12642 (2021).
- ⁵ A.L. Yarin, "Drop impact dynamics: splashing, spreading, receding, bouncing...," *Annu. Rev. Fluid Mech.* **38**(1), 159–192 (2006).
- ⁶ C. Josserand, and S.T. Thoroddsen, "Drop impact on a solid surface," *Annu Rev Fluid Mech* **48**(1), 365–391 (2016).
- ⁷ R.-J. Yang, H.-H. Hou, Y.-N. Wang, and L.-M. Fu, "Micro-magnetofluidics in microfluidic systems: A review," *Sens Actuators B Chem* **224**, 1–15 (2016).
- ⁸ R.K. Shah, and S. Khandekar, "Manipulation of Taylor bubble flow in a magneto-fluidic system," *Colloids Surf A Physicochem Eng Asp* **593**, (2020).
- ⁹ R.K. Shah, J.K. Drave, and S. Khandekar, "Thermal Transport in Laminar Convective Flow of Ferrofluids in the Presence of External Magnetic Field," *J Heat Transfer* **143**(6), (2021).

- ¹⁰ R.K. Shah, and S. Khandekar, "Influence of external magnetic manipulation on thermal transport characteristics of the bubble-slug flow of ferro-nanocolloids," *Colloids Surf A Physicochem Eng Asp* **646**, 128936 (2022).
- ¹¹ M. Kole, R.K. Shah, and S. Khandekar, "Energy efficient thermal management at low Reynolds number with air-ferrofluid Taylor bubble flows," *International Communications in Heat and Mass Transfer* **135**, 106109 (2022).
- ¹² R.K. Shah, and S. Khandekar, "On-demand augmentation in heat transfer of Taylor bubble flows using ferrofluids," *Appl Therm Eng* **205**, (2022).
- ¹³ R.K. Shah, and S. Khandekar, "Exploring ferrofluids for heat transfer augmentation," *J Magn Magn Mater* **475**, (2019).
- ¹⁴ J.V.I. Timonen, M. Latikka, L. Leibler, R.H.A. Ras, and O. Ikkala, "Switchable static and dynamic self-assembly of magnetic droplets on superhydrophobic surfaces," *Science* (1979) **341**(6143), 253–257 (2013).
- ¹⁵ X. Liu, N. Kent, A. Ceballos, R. Streubel, Y. Jiang, Y. Chai, P.Y. Kim, J. Forth, F. Hellman, S. Shi, P. Fischer, and T.P. Russell, "Reconfigurable ferromagnetic liquid droplets," *Science* (1979) **365**(6450), 264–267 (2019).
- ¹⁶ N. Lazarus, S.S. Bedair, and G.L. Smith, "Creating 3D printed magnetic devices with ferrofluids and liquid metals," *Addit Manuf* **26**, 15–21 (2019).
- ¹⁷ A. Ahmed, A.J. Qureshi, B.A. Fleck, and P.R. Waghmare, "Effects of magnetic field on the spreading dynamics of an impinging ferrofluid droplet," *J Colloid Interface Sci* **532**, 309–320 (2018).
- ¹⁸ A. Ahmed, B.A. Fleck, and P.R. Waghmare, "Maximum spreading of a ferrofluid droplet under the effect of magnetic field," *Physics of Fluids* **30**(7), 077102 (2018).
- ¹⁹ J. Zhou, and D. Jing, "Effects of vertical magnetic field on impact dynamics of ferrofluid droplet onto a rigid substrate," *Phys Rev Fluids* **4**(8), (2019).
- ²⁰ M.R. Hassan, and C. Wang, "Spreading Dynamics of an Impinging Ferrofluid Droplet on Hydrophilic Surfaces under Uniform Magnetic Fields," *Langmuir* **37**(45), 13331–13345 (2021).
- ²¹ Q.-P. Li, Y. Ouyang, X.-D. Niu, Y. Jiang, M.-F. Wen, Z.-Q. Li, M.-F. Chen, D.-C. Li, and H. Yamaguchi, "Maximum Spreading of Impacting Ferrofluid Droplets under the Effect of Nonuniform Magnetic Field," *Langmuir* **38**(8), 2601–2607 (2022).
- ²² J.-C. Huang, T.-Y. Han, J. Zhang, and M.-J. Ni, "Numerical Simulation of Maximum Spreading of an Impacting Ferrofluid Droplet under a Vertical Magnetic Field," *Langmuir* **40**(40), 20859–20871 (2024).
- ²³ J.D. Benthier, B. Wilson, P.A. Petrini, P. Lappas, and G. Rosengarten, "Ferrofluid droplet impingement cooling of modified surfaces under the influence of a magnetic field," *Int J Heat Mass Transf* **215**, (2023).
- ²⁴ J. Kim, "Phase-Field Models for Multi-Component Fluid Flows," *Commun Comput Phys* **12**(3), 613–661 (2012).
- ²⁵ S. Santra, S. Mandal, and S. Chakraborty, "Phase-field modeling of multicomponent and multiphase flows in microfluidic systems: a review," *Int J Numer Methods Heat Fluid Flow* **31**(10), 3089–3131 (2021).

- ²⁶ D. Jacqmin, "Contact-line dynamics of a diffuse fluid interface," *J Fluid Mech* **402**, 57–88 (2000).
- ²⁷ D. Jacqmin, "Calculation of Two-Phase Navier–Stokes Flows Using Phase-Field Modeling," *J Comput Phys* **155**(1), 96–127 (1999).
- ²⁸ P. YUE, J.J. FENG, C. LIU, and J.I.E. SHEN, "A diffuse-interface method for simulating two-phase flows of complex fluids," *J Fluid Mech* **515**, 293–317 (2004).
- ²⁹ P. Yue, C. Zhou, and J.J. Feng, "Spontaneous shrinkage of drops and mass conservation in phase-field simulations," *J Comput Phys* **223**(1), 1–9 (2007).
- ³⁰ P. YUE, C. ZHOU, and J.J. FENG, "Sharp-interface limit of the Cahn–Hilliard model for moving contact lines," *J Fluid Mech* **645**, 279–294 (2010).
- ³¹ H. Ding, P.D.M. Spelt, and C. Shu, "Diffuse interface model for incompressible two-phase flows with large density ratios," *J Comput Phys* **226**(2), 2078–2095 (2007).
- ³² X. Cai, M. Wörner, H. Marschall, and O. Deutschmann, "Numerical study on the wettability dependent interaction of a rising bubble with a periodic open cellular structure," *Catal Today* **273**, 151–160 (2016).
- ³³ X. Cai, M. Wörner, H. Marschall, and O. Deutschmann, "CFD Simulation of Liquid Back Suction and Gas Bubble Formation in a Circular Tube with Sudden or Gradual Expansion," *Emission Control Science and Technology* **3**(4), 289–301 (2017).
- ³⁴ F. Bai, X. He, X. Yang, R. Zhou, and C. Wang, "Three dimensional phase-field investigation of droplet formation in microfluidic flow focusing devices with experimental validation," *International Journal of Multiphase Flow* **93**, 130–141 (2017).
- ³⁵ P. Yue, C. Zhou, and J.J. Feng, "Sharp-interface limit of the Cahn–Hilliard model for moving contact lines," *J Fluid Mech* **645**, 279–294 (2010).
- ³⁶ N. Samkhaniani, A. Stroh, M. Holzinger, H. Marschall, B. Frohnäpfel, and M. Wörner, "Bouncing drop impingement on heated hydrophobic surfaces," *Int J Heat Mass Transf* **180**, 121777 (2021).
- ³⁷ C. Guo, D. Maynes, J. Crockett, and D. Zhao, "Heat transfer to bouncing droplets on superhydrophobic surfaces," *Int J Heat Mass Transf* **137**, 857–867 (2019).
- ³⁸ R.K. Shah, and S. Khandekar, "Heat transfer augmentation in ferrofluids in presence of external magnetic fields," in *International Conference on Computational Methods for Thermal Problems*, (2018).
- ³⁹ M. Wörner, "Numerical modeling of multiphase flows in microfluidics and micro process engineering: a review of methods and applications," *Microfluid Nanofluidics* **12**(6), 841–886 (2012).
- ⁴⁰ H. Hua, J. Shin, and J. Kim, "Level Set, Phase-Field, and Immersed Boundary Methods for Two-Phase Fluid Flows," *J Fluids Eng* **136**(2), (2013).